A Coupled Finite Element EHL and Continuum Damage Mechanics for Rolling Contact Fatigue

Neil R. Paulson[1]
Ph.D. Graduate Research Assistant
Email: npaulson@purdue.edu

Farshid Sadeghi[1*]
Cummins Distinguished Professor of Mechanical Engineering
Fellow, ASME, STLE Email: sadeghi@ecn.purdue.edu

Wassim Habchi[2]
Associate Professor of Mechanical Engineering
Email: wassim.habchi@lau.edu.lb

[1]*Purdue University*
School of Mechanical Engineering
West Lafayette, IN 47907, US

[2]*Lebanese American University*
Department of Industrial and Mechanical Engineering
Byblos, Lebanon

[*]Corresponding Author

Abstract

The objectives of this study were to investigate the effects of elastohydrodynamic lubrication pressure on the rolling contact fatigue life of non-conformal contacts. In order to achieve the objectives a finite element elastohydrodynamic lubrication (EHL) model was coupled with a continuum damage mechanics model. The coupled finite element damage mechanics and EHL (DMEHL) model was then used to investigate the effects of speed and damage variable on the fatigue life of non-conformal contacts. The results demonstrate that the damage variable has a significant effect on pressure distribution within the contact and depending on the level of damage; the pressure distribution can significantly deviate from the undamaged EHL pressure. The results also demonstrated that speed has a significant effect on fatigue and failure. A parametric study was conducted to examine the effects of the damage variable on the progression of fatigue and evolution of the EHL pressure profile. The results demonstrate that the critical damage value is important to fatigue and can drastically affect the EHL pressure profiles.

Keywords: rolling contact fatigue, Elastohydrodynamic Lubrication, damage mechanics

Introduction

Rolling contact fatigue (RCF) is the predominant mode of failure in properly lubricated, maintained and installed rolling element bearings (REB) [1]. There are two main modes of RCF failures, surface and subsurface initiated. In surface initiated RCF failure, a fatigue crack initiates on the surface and then propagates along a shallow path below the surface. This type of RCF failure is known to occur due to high friction [2] on the surface from dents, poor surface finishes, or insufficient lubrication conditions. In contrast to surface initiated RCF failures which usually can be controlled through proper lubrication and operation, subsurface initiated fatigue has not been shown to be preventable by design or operating conditions [3]. In the subsurface initiated RCF, the fatigue cracks occur below the surface of the component and are driven by the shear stress reversal. It is commonly believed that once a crack initiates, it will continue to propagate until it reaches the surface and forms an RCF spall, leading to increased vibration and failure of the component.

Subsurface initiated RCF has garnered a significant amount of interest in the tribology community over the past few decades. Lundberg and Palmgren [4] published the first significant paper in the prediction of subsurface RCF, where they identified the alternating component of the shear stress to be the critical stress that initiates fatigue damage. Lundberg and Palmgren's [1] landmark publication is still significant today as both the ISO and ASME standards are derived from their work. Lundberg and Palmgren's model relies on experimental results to fit the model parameters for the fatigue life equation [1]. The need for fitting experimental results is due in a significant part to the variation seen in rolling contact fatigue spall formation. In the past few decades, RCF models have been primarily empirical, stress based and included probability and scatter through an assumed Weibull distribution function. A few researchers have also proposed deterministic stress based models that predict life and do not incorporate the scatter in life [5]. Raje et al. [6] proposed an alternative approach which accounted for the microstructural variation in material and thus introduced statistical nature of rolling contact fatigue through modeling. Using this model, a given microstructure has a deterministic fatigue life; however, Raje and others [7–9] have shown that by agglomerating many different microstructures fatigue lives for a given set of contact conditions, the stochastic nature of the experimental results can be observed using a purely analytical model. Since its first publication, this modeling approach has been extended to address 3D microstructural models [6, 9, 10], plasticity effects [11], residual stresses [12] and anisotropy of material [13].

Microstructural models have been used extensively and shown great potential for RCF modeling by demonstrating the ability to predict RCF life and scatter. While many of the limitations of original bearing models have been eliminated by this approach, one assumption that remains is nearly all RCF models use a constant Hertzian pressure to approximate the applied load. However, invariably all machine elements subject to rolling contact fatigue are lubricated and therefore the pressure distribution in these contacts is significantly different than that of Hertzian

and governed by the elastohydrodynamic lubrication (EHL) regime. In EHL, the variation of the pressure is more gradual in the inlet of the contact due to the wedge effect created by the contact geometry. Near the outlet of the contact, the pressure displays a spike followed by a steep drop as the contact geometry diverges. EHL has been investigated extensively over the last sixty years or so. In the standard formulation of EHL models, the elastic deformation is calculated using the influence coefficient method [14, 15]. Xu et al. [16] incorporated the standard finite difference EHL equations with finite element method to determine plastic deformation in the contact region. Habchi et al. [17] developed a FEA approach that fully couples the finite element model solving the elasticity and Reynolds equations simultaneously. By incorporating the elasticity through finite elements, the stress distributions below the contact surface can be determined, which is critical for calculating RCF crack formation. Cerullo [18] recently investigated the differences between RCF life predictions using EHL and Hertzian pressure profiles. This work used the Dang van fatigue criterion to predict RCF lives showing that in a pristine contact, with no inclusions or surface roughness, the EHL pressure doubled the RCF life. Using EHL models to generate the pressure profiles also allows for the velocity effects on pressure distribution to be considered. As contact velocities increase, the EHL pressure profile deviates significantly from the Hertzian contact prediction [14].

In this paper, a finite element EHL model was developed and combined with continuum damage mechanics (CDM) to investigate the effects of EHL on RCF. By coupling EHL and CDM, the effects of speed and lubricant properties on pressure and consequently RCF can be critically examined. It is also to be noted that, because the EHL pressure is reevaluated throughout the fatigue process, the evolution of the pressure during the fatigue damage process can be investigated. The evolution of pressure was investigated for a variety of critical damage values, demonstrating the importance of this parameter in RCF.

Modeling Approach

In order to determine the effects of lubrication on rolling contact fatigue, a model was developed that couples the hydrodynamic lubrication, elastic deformation and continuum damage mechanics of the contacting surfaces. A fully coupled FE model which includes the Reynolds and elasticity equations was used to determine the internal stresses acting in the contacting bodies. The CDM model was then used to assess the degradation of the materials during the fatigue process. Voronoi tessellation was used to generate a refined computational mesh to accurately calculate the EHL pressure and damage within the contact. Figure 1 depicts the flowchart for the coupled damage mechanics and EHL (DMEHL) model developed for this investigation. The modeling begins with the discretization of the domain using the Voronoi tessellation. The discretized domain is then used by the FE EHL model to determine the pressure, film thickness and stresses which are passed to the CDM model. The damage variable for each element is updated by the CDM model and returned to the FE EHL model. The process continues until a damage element occurs on the surface and the process is then stopped.

EHL Finite Element Model

An FE EHL model similar to Habchi et al. [17] was developed and coupled with CDM to account for RCF damage. A basic description of the model is described below. For a more complete description, please refer to [17] and [19].

Reynolds Equation

The line contact isothermal Newtonian steady-state Reynolds equation [20] including the modification for free boundary condition by Wu [xx] is given by

$$\frac{\partial}{\partial \mathrm{X}}\left(\epsilon \frac{\partial P}{\partial X}\right) - \frac{\partial(\bar{\rho}H)}{\partial X} - \xi \min(P, 0) = 0 \tag{1}$$

where

$$\epsilon = \frac{\bar{\rho}H^3}{\bar{\mu}\lambda}, \lambda = \frac{12v\mu_0 r^2}{b^3 p_h}$$

The Reynolds equation is solved along the upper contact surface of the domain Ω_c, and the resulting pressure distribution is used to define the boundary condition for the elastic deformation equation. The last term in the Reynolds equation, $\xi \min(P, 0)$, is a penalty term used to drive negative pressures to zero. The outlet of the contact creates a free boundary problem where the pressure will go to zero. Unlike the finite difference approach, negative pressures cannot be simply set to zero since all of the pressure unknowns update simultaneously. ξ in equation (1) is set to an arbitrarily large constant to drive pressure to zero in negative pressure regions.

The Reynolds equation (1) requires knowledge of the film thickness (H) for the bounding surfaces. For two cylindrical bodies in contact the non-dimensional film thickness equation is given as;

$$H = H_0 + \frac{X^2}{2} - U_y \tag{2}$$

Where H_0 is the non-dimensional rigid body separation between the rolling elements, X is the non-dimensional distance from the contact centerline, and U_y is the non-dimensional displacement at the desired location calculated from the elastic equation.

The non-dimensionalized density [21] and viscosity [22] variation with respect to pressure are given by;

$$\bar{\rho} = 1 + \frac{0.6 * 10^{-9} P}{P_h + 1.7 * 10^{-9} P} \tag{3}$$

$$\bar{\mu} = e^{(\ln(\mu_0)+9.67)\left(-1+\left(1+5.1*10^{-9}P*P_h\right)^{Z_0}\right.} \tag{4}$$

Where,

$$Z_0 = \frac{\alpha}{5.1 * 10^{-9}(\ln(\mu_r) + 9.67)}$$

Elasticity Equation

In order to determine the deformation (U_y) as well as the stresses throughout the domain, the elasticity equations must be solved:

$$\nabla \cdot (C\nabla \mathrm{U}) = 0 \tag{5}$$

With the boundary conditions

$$U = 0 \; on \; the \; bottom \; surface$$

$$\sigma_y = -P \text{ The}$$

$$E_{eq} = \frac{E_1 E_2}{E_1 + E_2} \frac{b}{r p_h}$$
$$\nu_{eq} = \frac{\nu_1 E_2 + \nu_2 E_1}{E_1 + E_2} \tag{6}$$

Load Balance Equation

The final equation to be solved is the global load balance equation:

$$\int_{\Omega_c} P d\Omega = \frac{\pi}{2} \tag{7}$$

This equation imposes that the correct load is applied and is the final equation to allow the adjustment of rigid body separation, H_0, of the contacting bodies.

Finite Element Formulation

Equations (1), (5) and (7) were formulated using the Galerkin method by multiplying them by the appropriate weighting function, integrating by parts and removing null boundary conditions. The systems of equations thus become;

$$\begin{cases} \int_{\Omega_c} -\epsilon \frac{\partial P}{\partial X} \cdot \frac{\partial W_P}{\partial X} d\Omega + \int_{\Omega_c} \bar{\rho} H \frac{\partial W_P}{\partial X} - \int_{\Omega_c} \xi \cdot \min(P, 0) \, W_P d\Omega = 0 \\ \int_{\Omega} -C \, \nabla U \cdot \nabla W_U d\Omega + \int_{\Omega_c} -P \cdot W_{U_y} = 0 \\ \int_{\Omega_c} P W_{H_0} d\Omega - \frac{\pi}{2} W_{H_0} = 0 \end{cases} \tag{8}$$

The Galerkin form is then solved by discretizing the linear elasticity problem into linear strain triangles which corresponding projections over the contact domain Ω_c are used to discretize the

hydrodynamic problem. To solve the nonlinear Reynolds equation, a modified Newton-Raphson procedure was used. All equations in (8**)** are linearized with respect to each of the independent variables. The Reynolds equation is dependent on $P,\ U\ and\ H_0$ while the elasticity equation is dependent on P and U and the load balance is only dependent on the pressure P. The load balance equation is incorporated into the system of equations (8) as an ordinary integral equation along with the addition of H_0 as the corresponding unknown. The Newton-Raphson system of equations to solve at every iteration *i* thus becomes:

$$\begin{bmatrix} J_{11} & J_{12} & J_{13} \\ J_{21} & J_{22} & 0 \\ J_{31} & 0 & 0 \end{bmatrix}^{i-1} \begin{Bmatrix} \delta P \\ \delta U \\ \delta H_0 \end{Bmatrix}^{i} = \begin{bmatrix} -R \\ -J_{21}P - J_{22}U \\ \frac{\pi}{2} - J_{31}P \end{bmatrix}^{i-1} \tag{9}$$

Where J_{11} is the partial derivative of the Reynolds equation with respect to P; J_{12} is the partial derivative of the Reynolds equation with respect to U, etc. R is the residual of Reynolds equation. The Reynolds equation is stabilized using the Streamline Upwind Petrov Galerkin (SUPG) method [23]. This derivation is omitted from the current paper for brevity and the reader is referred to Habchi [19] for a complete description of the stabilization procedure.

While the above FE model is sufficient to determine the stress distribution at a fixed point in the model, the stresses within the body must be calculated over the entire rolling pass to determine how the stresses change due to the fatigue process. In order to determine this stress condition, the elastohydrodynamic pressure was traversed across the surface of a representative volume element in 21 steps moving from the right to left of the domain as shown in Figure 2. To approximate a semi-infinite domain the extents of the computational domain was chosen to be 60b by 60b; however, to limit the computational effort, the continuum damage mechanics model calculations were limited to a sub-region as described by Bomidi et al [10]. This sub-region is limited to -2b to 2b across and -1.5b deep.

Continuum Damage Mechanics Model

Continuum damage mechanics is used to determine the deterioration of material due to the initiation and growth of microvoids in the material [24]. Damage mechanics theory attempts to simplify the microscopic mechanism (i.e. slip planes and dislocation movement) into an empirical relationship applied on the mesoscale. The effects of the microscale failure are captured by the introduction of a damage variable, D, which affects the constitutive relationship of the modeled material. In general the damage variable is a tensor; however, for the case of isotropic damage [7, 10, 25] D becomes a scalar. For a plane strain homogenous isotropic material the stress strain including damage is given by (Lemaitre [24]);

$$\sigma_{ij} = \frac{E(1-D)}{1+\nu}\left(\epsilon_{ij} + \frac{\nu}{1-2\nu}\epsilon_{kk}\delta_{ij}\right) \tag{10}$$

where δ_{ij} is the Kronecker delta function. The damage variable, D, is initially zero for an undamaged material. Using this value, equation (10) simplifies to the standard elastic plane strain equation. As the material deteriorates, the damage variable increases and the material becomes increasingly compliant until, at the limiting value of 1, the material has no resistance to deformation. While equation (10) describes the stress-strain and damage state in the material; an additional equation is required to determine how the damage evolves due to the continuous stress cycles. Raje et al. [6] modified the damage evolution model proposed by Lemaitre [24] to account for shear stress reversal as the critical stress. The damage evolution equation is given by;

$$\frac{dD}{dN} = \left[\frac{\Delta\tau}{\tau_r(1-D)}\right]^m \tag{11}$$

where $\Delta\tau$ is the shear stress reversal at the grain boundary, τ_r is the shear resistance stress representing the material's ability to resist fatigue damage, N is the number of cycles, $\Delta\sigma$ is the range of the fatigue stress, and m is the damage exponent. Both τ_r and m are experimentally determined material dependent parameters.

The two material damage parameters used in this study were determined using the approach described by Slack et al. [8]. These results were calculated using torsion fatigue results for ANSI-52100 bearing steel [26]. Using this approach, the damage parameters were determined as:

$$m_1 = 10.1$$

$$\tau_{r,1} = 6.113\ MPa$$

These values were calculated using a maximum value of damage, D_{crit}, equal to 1; however, Warhatpande et al. [27] estimated that the D_{crit} for ANSI 4142 steel is 0.12. Therefore, this research considered alternative D_{crit} values. To determine the corresponding material parameters, the equation presented by Walveker et al. [28] described below was used in this investigation:

$$\tau_r = A\left[\frac{1}{m+1} - \frac{(1-D_{crit})^{m+1}}{m+1}\right]^{-\frac{1}{m}} \tag{12}$$

Where A is a constant that can be calculated from m_1 and $\tau_{r,1}$. From Equation (12), the material parameters can be derived for different critical damage values from the same fatigue results.

Because RCF lives are typically in the millions of cycles, it is computationally infeasible to simulate every cycle. Thus, Lemaitre [24] developed an approach to extrapolate the fatigue damage calculated in one computational load pass. The method assumes piecewise periodic loading that is constant over a block of cycles. The number of cycles in a given block is

calculated by selecting a damage increment ΔD_{lim} and calculating the number of cycles required to reach this damage value by:

$$\Delta N = \frac{\Delta D_{lim}}{\left(dD/dN\right)_{crit}} \tag{13}$$

Where ΔD_{lim} is the specified change in damage, and $\left(dD/dN\right)_{crit}$ is the maximum damage rate calculated in the given load pass.

Voronoi Tessellation

Voronoi tessellations have been extensively used to model microstructure of polycrystalline materials [29, 30]. In order to generate a Voronoi space, nucleation points are randomly placed throughout the domain. The Voronoi polygons are then constructed by forming regions of material closest to a given seed point [31]. To insure that the generated microstructure matches the measurements of a typical bearing steel, the distribution of Voronoi seed points is set to a given mean grain size of 10μm [32].

While previous investigators [7–9, 12] have used the centroid of an N-sided Voronoi to divide into N finite elements, this approach is insufficient when the EHL pressure profiles must be solved. Due to the high gradients associated with the EHL pressure profile some areas within the domain need to be finely discretized; particularly in the pressure spike region where high resolution is required for convergence of the Reynolds equation. Figure 3 illustrates how the finite element sizes are varied while maintaining the Voronoi boundaries. The meshing software Triange [33] allows each Voronoi polygon to be defined in the domain. A maximum finite element size is then specified in each Voronoi polygon based on the requirements of the EHL problem. In addition, since the discretization requirements change as the pressure passes across the domain, a different maximum finite element size is set for each load step resulting in a unique finite element domain for each load step. Once the computational domains were generated, each finite element was assigned to a Voronoi element and the damage was assigned based on the corresponding Voronoi element damage.

Results & Discussions

In order to determine the applicability and capability of the current model for RCF investigation, an initial study was performed using the operating conditions as presented by Pan and Hamrock [14] and material damage parameters as described by Slack et al [8]. Table 1 contains the parameters used for this evaluation and study. For this test the critical damage was set to 0.99 as described in Slack et al [8]. Figure 4 depicts the results from the different load passes for the proposed case. Each one of the figures displays the damage field and contact pressure for various load passes. Figure 4a depicts the damage state within the domain (body) for the load pass 10. For this load pass two elements have been critically damaged. Figure 4b illustrates that after 10 more load passes (computational cycles), three more elements have reached the critical

damage level. At this point, all of the critically damaged elements are separate from each other in the RVE and have initiated near the critical shear stress reversal depth of 0.5b. After 50 load passes, Figure 4c, no new initiation points of damage are observed. Instead, the previous initiation points begin to grow as additional elements fail near the original initiation sites. The transition from individual damaged elements to growth of extended damaged regions demarcates the transition from fatigue initiation to stable propagation [34]. At load pass 100, shown in Figure 4d, the damaged elements have coalesced to form a long dominant fatigue crack. As the load passes increase, this dominant fatigue crack continues to grow and extend across the domain as is illustrated in Figure 4d and e. While the fatigue damage grows, significant changes are observed in the EHL pressure profile. The decreased stiffness of the coalesced damaged region causes the pressure to decrease directly above thedamaged region. This leads to both an increase in the width of the pressure profile and an increase in pressure over the undamaged material. Both phenomena are essential for preserving the equilibrium of forces over the EHL contact.. It is to be noted that the change in pressure profiles is not observed in the initiation phase of the fatigue growth as Figure 4a and b illustrate no noticeable differences from the original EHL pressure profile. During propagation, the decrease in pressure over the damaged region will contribute to the crack growth by increasing pressure on the left and right sides of the damaged region. This phenomenon is seen in the progression of damage from load pass 100 to 500 (see Figure 4d through f) as the damaged region expandssteadily towards the maximum pressure regions.

Figure 4 illustrates the damage and pressure distribution at the center of the RVE (load step 11) for different load passes. However, each load pass consists of 21 load steps, thus it is important to examine the load steps across the domain for a particular damage state as shown in Figure 5. The first and last load steps (Figure 5a and f) demonstrate that pressure profiles at the extreme edges of the loading region are negligibly affected by the damage state in the RVE region. This demonstrates that the contact must be directly over the damaged region for the decrease in stiffness to have an effect on the EHL pressure. Load steps 5 through 17 show a perturbation in the pressure when the contact is directly over the damaged region. In load step 5, as shown in Figure 5b, the damage region is located in the inlet zone of the contact leading to an extension of the inlet pressure. Figure 5c through e depict the load steps 9 through 17, which demonstrate a decrease in the pressure directly above the critically damaged region. All of these perturbations in pressure will cause an increase in load supported by the undamaged material directly adjacent to the critically damaged region, contributing to the crack propagation described by Figure 4.

As noted earlier, the EHL pressure is distinctly different than that of the Hertzian pressure. Most previously published work on RCF used a constant Hertzian pressure to obtain probability of failure and life. Thus, in order to determine the effects of the EHL pressure on rolling contact fatigue, it was compared to a constant Hertzian pressure. The same conditions as described in Table 1 were used in this comparison. Before comparing the damage profiles and predicted fatigue lives, it is warranted to examine the differences between a Hertzian and EHL pressure

profile when no damage is present. The Hertzian pressure profile, the dotted line in Figure 6, has a steep pressure gradient at X = -1; by contrast the EHL pressure profile, solid line has a more gradual and gentle gradient into the contact zone ($X \leq -1$) on the inlet side of the contact. The differences between the two pressure profiles are more prominent on the outlet side ($X \approx 1$) of the contact. The Hertzian pressure is perfectly symmetric with respect to the center of the contact showing a steep pressure gradient at X = 1. The EHL pressure is not symmetric about the center of the contact (X = 0). Near the outlet region ($X \approx 1$), the EHL pressure exhibits a pressure spike immediately followed by a sharp drop in pressure and then a smooth transition to zero pressure at X > 1. These differences in pressure profiles will result in EHL having an asymmetric shear stress profile as opposed to the symmetric Hertzian shear stress profile. Also the smoother transition on the inlet side of the contact will decrease the shear stress in that region while the steep pressure spike will increase the shear stress in the contact outlet. Figure 7 provides a comparison between the internal damage distributions of the Hertzian and DMEHL models. The damage distributions for both 50 and 100 load passes are nearly identical; however, the damage distributions deviate at the 200th load pass. The damage distribution for the EHL pressure displays a gradual growth towards the contact surface while the Hertzian pressure has a much steeper, nearly vertical path to the surface (Figure 7e and f). The difference in fatigue growth between the two approaches is explained by the fixed pressure profile of the Hertzian model. Since the Hertzian pressure remains constant regardless of the damage, this high pressure forms high stresses resulting in damage propagating from the middle of the damaged region to the surface. As described previously, the fatigue damage growth in the EHL model is propagated towards the left and right sidesof the damaged region due to decreased stresses directly over the critically damaged domain.

In the previous paragraph, the differences between the RCF lives from the current DMEHL and a constant Hertzian pressure were discussed and contrasted. It is of interest to investigate the condition where an EHL pressure which is not updated due to damage and remains constant through the damage process, similar to the case discussed in Figure 7. Using this constant pressure profile allows the differentiation between the effect of the EHL pressure profile and the effect of updating pressure during the simulation. As noted earlier, initiation occurs when the first element reaches the critical level of damage and final life is reached when a critically damaged element reaches the surface [8, 25]. Table 2 contains the results for the initiation and final life for all three cases studied. Comparing the two constant pressure models, the EHL pressure predicts longer lives than the Hertzian pressure for both initiation and final life. The 3.7% increase in initiation and the 7.1% in final lives are attributed solely to the difference in the pressure distributions shown in Figure 6. The constant EHL pressure was then compared to the dynamically updated EHL pressure. The initiation lives of these two cases show a negligible difference since the damage accumulation has a minimal effect on the pressure distribution in the initiation stage. However, the final life is affected by the pressure update, increasing the final life by 7.0% compared to the constant EHL pressure case. This extension of fatigue life is

attributed to a long, gradual growth of fatigue damage shown in Figure 4. This is due to pressure decrease above damaged regions as discussed earlier. A similar increase in final life was observed by Bomidi et al. [35] when damage updated contact pressure model was compared to a constant Hertzian stress model. By combining both the EHL pressure profile and the pressure update, the DMEHL model extends the final life prediction by 16.7% compared to the Hertzian model proposed by Slack and Sadeghi [8, 25].

The results described previously were obtained for the same rolling velocity; however, the EHL model allows the speed to be adjusted. Speed has a significant effect on the pressure and thus will affect the calculated RCF lives. Three different non-dimensional speeds ranging from U = 10^{-12} to 10^{-10} were investigated using DMEHL. Figure 8 depicts the pressure distributions and damage profiles for these speed cases. In the higher speed EHL case, the pressure builds more gradually in the inlet region while the pressure spike at the outlet is more pronounced. The pressure profiles show marked differences, however the damage profiles are nearly identical for the three different speeds as observed. This indicates that the shear stress for the three different cases has a similar profile. Table 3 contains the initiation and propagation lives of the three different speed cases. The results indicate that higher speeds increase the RCF life. The difference in lives between the lowest speed 10^{-12} and highest speed 10^{-10} are 7% for the initiation life and 23% for the final fatigue lives. The increase of fatigue life as speed increases is in agreement with the results from Cerullo [18] as well as the ISO and ASME [36] speed adjustment factors. It is observed that while the final life (stress cycles) increases, this does not mean the component will last a longer time as the increased speed will also increase the stress cycling rate. While the life differences shown are significant, the speed differences are large (100 times faster) between the three cases and would likely correlate to different rolling element applications in service.

In the previous sections, the investigated effects corresponded to a critical damage level = 0.99. However, the critical damage value can be significantly lower [24, 27, 28] than 0.99. Thus, to understand what role the critical damage value plays in the DMEHL model, four different critical damage values (0.125 to 0.99) were studied. Because the only difference between the four cases was the critical damage value; each test case has an identical stress distribution to begin the simulation. Figure 9 shows the pressure profiles and damage after 100 load passes. The pressure profiles for the critical damage value of 0.125 and 0.25, Figure 9a and b, show a negligible difference. Figure 9c with a critical damage value of 0.5 shows a slight flattening of the pressure profile at the center of the contact due to damage accumulation in the middle of the domain. Figure 9d illustrates a clear decrease in pressure over the critically damaged region. This demonstrates that the damage model proposed is dependent on the critical damage. While it is clear from previous results that the damage affects the pressure profile, significant analysis must be undertaken to assure the critical damage is set to an appropriate level.

Summary and Conclusion

In this investigation, a finite element EHL model was combined with continuum damage mechanics (CDM) to determine the effects of EHL on RCF. By coupling EHL and CDM, the effects of speed on pressure and consequently RCF was examined. Results from the DMEHL model were compared to a Hertzian pressure damage model. The comparison indicates there is a significant difference in fatigue lives between the DMEHL and Hertzian models due to both the EHL pressure profile as well as the pressure changes due to damage accumulation. The 3.7% increase in initiation life and 7.1% increase in final life were attributed solely to the differences between the constant EHL and Hertzian pressure distributions. However, the pressure update due to damage accumulation of the DMEHL model contributed to a 7.0% increase in the final life over a constant EHL pressure. When both effects were combined, a 16.7% increase in final life was observed. This variation indicates an under-prediction of the fatigue lives when not accounting for the EHL pressure profile and pressure changes due to damage accumulation.

The model was also used to determine the effects of speed on the fatigue lives and damage accumulation. Results demonstrate that increased speed has a positive effect on the fatigue lives. An increase in final lives of 23% was observed when the lowest and highest speeds were compared. However, this does not mean the component will last a longer time as the increased speed will also increase the stress cycling rate. It was also found that speed had little effect on the shape or size of the fatigue damage generated in the domain. Finally, the effect of the critical damage value was evaluated for the coupled DMEHL. The results illustrate that the variations in the pressure profiles are significantly affected by the level of critical damage. If the critical damage value is decreased below 0.5, the damage showed a negligible effect on the pressure profiles while higher damage values showed significant changes in the pressure profile. This illustrates the importance of setting the critical damage level for a given material when using the DMEHL model.

Acknowledgements

The authors would like to express their deepest appreciations to Cummins Inc. for their generous support of this project.

References

[1] Sadeghi, F., Jalalahmadi, B., Slack, T. S., Raje, N., and Arakere, N. K., 2009, "A Review of Rolling Contact Fatigue," J. Tribol., **131**(4), p. 041403.

[2] Zhou, R. S., Cheng, H. S., and Mura, T., 1989, "Micropitting in Rolling and Sliding Contact Under Mixed Lubrication," J. Tribol., **111**(October), pp. 605–613.

[3] Ioannides, E., and Harris, T. A., 1985, "A New Fatigue Life Model for Rolling Bearings," J. Tribol., **107**, pp. 367–377.

[4] Lundberg, G., and Palmgren, A., 1947, "Dynamic Capacity of Rolling Bearings," Acta Polytech. Mech. Eng. Ser., **1**(3), pp. 1–52.

[5] Weinzapfel, N., and Sadeghi, F., 2013, "Numerical modeling of sub-surface initiated spalling in rolling contacts," Tribol. Int., **59**, pp. 210–221.

[6] Raje, N., Sadeghi, F., Rateick, R. G., and Hoeprich, M. R., 2008, "A Numerical Model for Life Scatter in Rolling Element Bearings," J. Tribol., **130**(1), p. 011011.

[7] Weinzapfel, N., Sadeghi, F., Bakolas, V., and Liebel, A., 2011, "A 3D Finite Element Study of Fatigue Life Dispersion in Rolling Line Contacts," J. Tribol., **133**(4), p. 042202.

[8] Slack, T., and Sadeghi, F., 2010, "Explicit finite element modeling of subsurface initiated spalling in rolling contacts," Tribol. Int., **43**(9), pp. 1693–1702.

[9] Jalalahmadi, B., and Sadeghi, F., 2009, "A Voronoi Finite Element Study of Fatigue Life Scatter in Rolling Contacts," J. Tribol., **131**(2), p. 022203.

[10] Bomidi, J. a. R., Weinzapfel, N., Sadeghi, F., Liebel, A., and Weber, J., 2013, "An Improved Approach for 3D Rolling Contact Fatigue Simulations with Microstructure Topology," Tribol. Trans., **56**(3), pp. 385–399.

[11] Warhadpande, A., Sadeghi, F., Kotzalas, M. N., and Doll, G., 2012, "Effects of plasticity on subsurface initiated spalling in rolling contact fatigue," Int. J. Fatigue, **36**(1), pp. 80–95.

[12] Warhadpande, A., Sadeghi, F., Evans, R. D., and Kotzalas, M. N., 2012, "Influence of Plasticity-Induced Residual Stresses on Rolling Contact Fatigue," Tribol. Trans., **55**(4), pp. 422–437.

[13] Paulson, N. R., Bomidi, J. a. R., Sadeghi, F., and Evans, R. D., 2014, "Effects of crystal elasticity on rolling contact fatigue," Int. J. Fatigue, **61**, pp. 67–75.

[14] Pan, P., and Hamrock, B. J., 1989, "Simple Formulas for Performance Parameters Used in Elastohydrodynamically Lubricated Line Contacts," **111**(April), pp. 246–251.

[15] Venner, C. H., and Lubrecht, A. A., 1991, "Numerical Simulation of the Overrolling of a Surface Feature in an EHL Line Contact," **113**(October).

[16] Xu, G., Nickel, D., Sadeghi, F., and Ai, X., 1991, "Thermoelastic Effects in Lubricated Roiling / Sliding Line Contacts," **210**.

[17] Habchi, W., Eyheramendy, D., Vergne, P., and Morales-Espejel, G., 2008, "A Full-System Approach of the Elastohydrodynamic Line/Point Contact Problem," J. Tribol., **130**(2), p. 021501.

[18] Cerullo, M., 2013, "Application of Dang Van criterion to rolling contact fatigue in wind turbine roller bearings under elastohydrodynamic lubrication conditions," Proc. Inst. Mech. Eng. Part C J. Mech. Eng. Sci., **228**(12), pp. 2079–2089.

[19] Habchi, W., 2008, “A Full-System Finite Element Approach to Elastohydrodynamic Lubrication Problems: Application to Ultra-Low-Viscosity Fluids.”
[20] Reynolds, O., 1886, “On the Theory of Lubrication and Its Applications to Mr. Beauchamp Tower’s Experiments, Including an Experimental Determination of the Viscosity of Olive Oil,” Proc. R. Soc. London, **40**, pp. 191–203.
[21] Dowson, B. D., and Higginson, G. R., 1959, “A Numerical Solution to the Elasto-Hydrodynamic Problem,” J. Mech. Eng. Sci., **1**(1).
[22] Roelands, C. J. A., 1966, “Correlational Aspects of the Viscoity-Temperature-Pressure Relationship of Lubricating Oils,” Technische Hogeschool Delft.
[23] Brooks, N., and Hughes, T., 1982, “Streamline Upwind/Petrov-Galerkin Formulations for Convection Dominated Flows with Particular Emphasis on the Incompressible Navier-Stokes Equations,” Comput. Methods Appl. Mech. Eng., **32**, pp. 199–259.
[24] Lemaitre, J., 1992, A Course on Damage Mechanics, Springer-Verlag, Berlin.
[25] Raje, N., and Sadeghi, F., 2009, “Statistical numerical modelling of sub-surface initiated spalling in bearing contacts,” Proc. Inst. Mech. Eng. Part J J. Eng. Tribol., **223**(6), pp. 849–858.
[26] Styri, H., 1951, “Fatigue Strength of Ball Bearing Races and Heat-Treated 52100 Steel Specimens,” Proceeds-American Soc. Test. Mater., **51**.
[27] Warhadpande, A., Jalalahmadi, B., Slack, T., and Sadeghi, F., 2010, “A new finite element fatigue modeling approach for life scatter in tensile steel specimens,” Int. J. Fatigue, **32**(4), pp. 685–697.
[28] Walvekar, A. a., Leonard, B. D., Sadeghi, F., Jalalahmadi, B., and Bolander, N., 2014, “An experimental study and fatigue damage model for fretting fatigue,” Tribol. Int., **79**, pp. 183–196.
[29] Zavattieri, P. D., and Espinosa, H. D., 2001, “Grain Level Analysis of Crack Initiation and Propagation in Brittle Materials,” Acta Mater., **49**, pp. 4291–4311.
[30] Ito, O., and R., F. E., 1993, “Computer Modelling of Anisotropic Grain Microstructure in Two Dimensions,” Acta Metall. Mater., **41**(1), pp. 191–198.
[31] Okabe, A., Boots, B., Sugihara, K., and Chiu, S. N., 2000, Spatial Tessellations, Wiley.
[32] Bomidi, J. A. R., Weinzapfel, N., Sadeghi, F., Slack, T., Moghaddam, S. M., Liebel, A., Weber, J., and Kreis, T., 2013, “Experimental and Numerical Investigation of Torsion Fatigue of Bearing Steel,” J. Tribol., **135**(3), p. 031103.
[33] Shewchuk, J. R., 1996, “Triangle: Engineering a 2D Quality Mesh Generator and Delaunay Triangulator,” Applied Computational Geometry: Towards Geometric Engineering, M.C.L. and D. Manocha, ed., Springer-Verlag, pp. 203–222.
[34] Leng, X., Chen, Q., and Shao, E., 1988, “Initiation and Propagation of Case Crushing Cracks in Rolling Contact Fatigue,” Wear, **122**, pp. 33–43.
[35] Bomidi, J. a. R., and Sadeghi, F., 2013, “Three-Dimensional Finite Element Elastic–Plastic Model for Subsurface Initiated Spalling in Rolling Contacts,” J. Tribol., **136**(1), p. 011402.
[36] ASME Tribology Division Technical Committee, 2003, “Life Ratings for Modern Rolling Bearings: A Design Guide for the Application of International Standard ISO 281/2,” ASME International, New York.

Table 1: Material and Operating Conditions

Parameter	Value
U	10^{-11}
W	$1.3*10^{-4}$
G	5000
E_1 and E_2	212 GPa
ν_1 and ν_2	0.30
P_{Hz}	1GPa
b	100μm

Table 2: Pressure distribution effect on fatigue life predictions

Model	Initiation Life	Final Life
Constant Hertzian Stress	$6.05*10^9$	$7.86*10^9$
Constant EHL Stress	$6.27*10^9$	$8.46*10^9$
Coupled DMEHL Stress	$6.27*10^9$	$9.13*10^9$

Table 3: Speed effects on fatigue life prediction obtained from DMEHL

Nondimensional Speed	Initiation Life	Final Life
10^{-12}	$6.05*10^9$	$8.49*10^9$
10^{-11}	$6.27*10^9$	$9.13*10^9$
10^{-10}	$6.52*10^9$	$1.05*10^{10}$

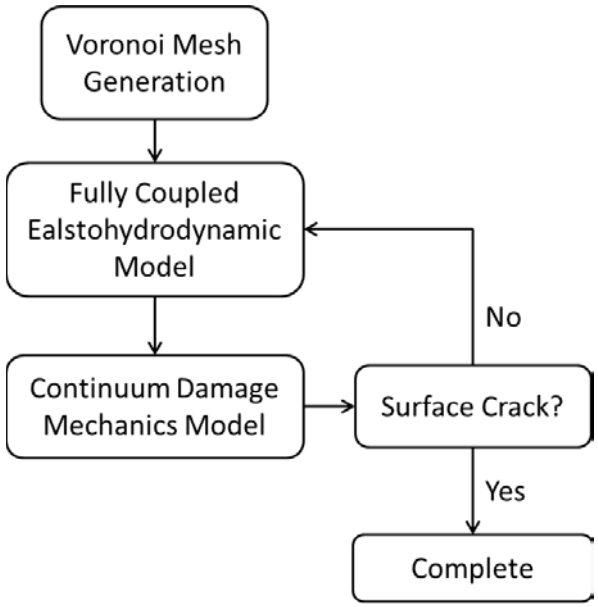

Figure 1: Diagram of DMEHL Model

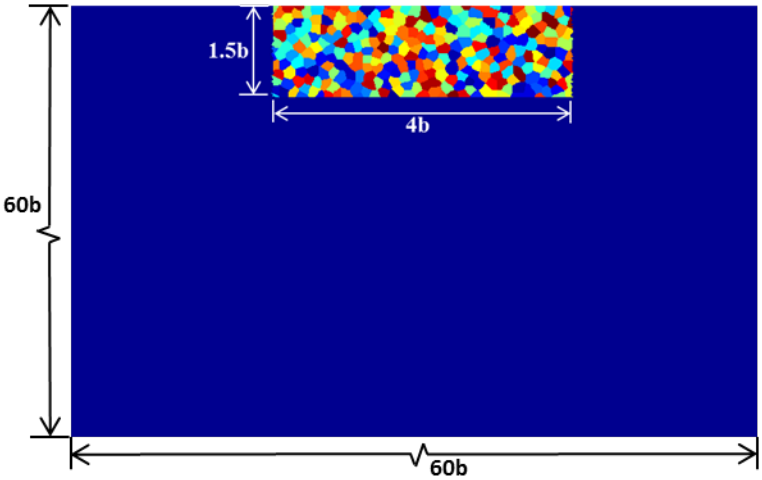

Figure 2: The entire computation domain is 60X60b while the representative volume of Voronoi elements is 1.5X4b. The pressure profiles are passed from right to left across the domain.

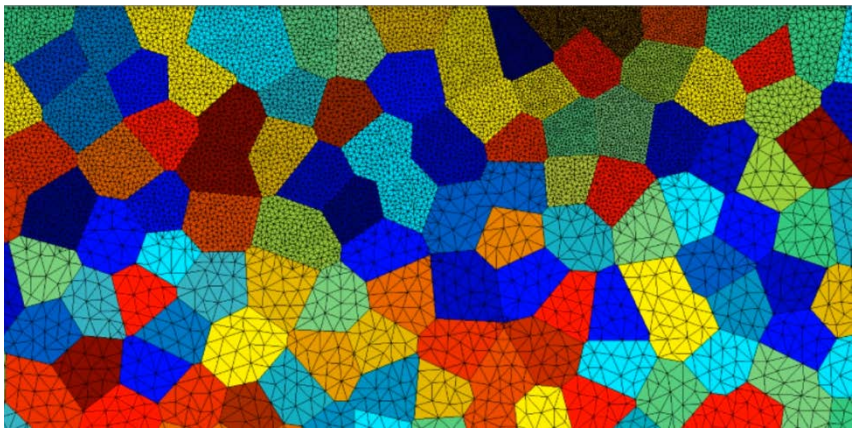

Figure 3: Size variation in FE domain.

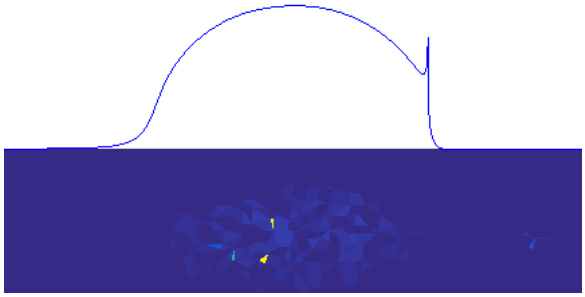

a) Load Pass 10

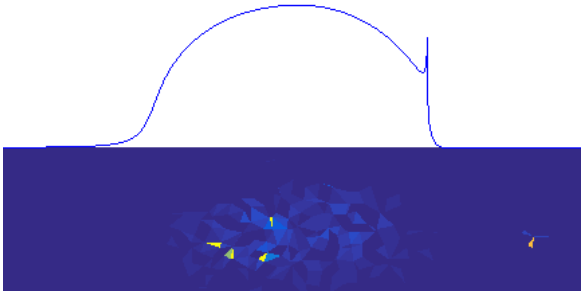

b) Load Pass 20

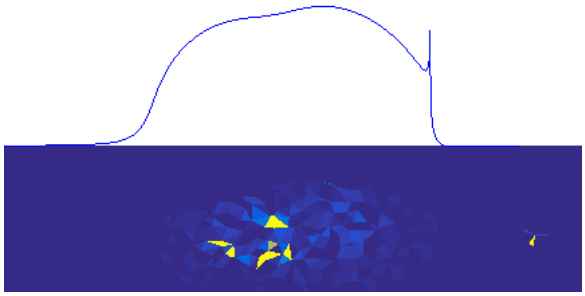

c) Load Pass 50

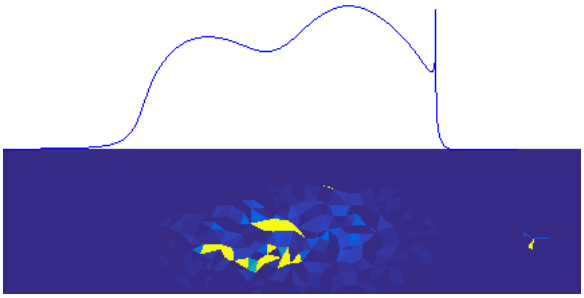

d) Load Pass 100

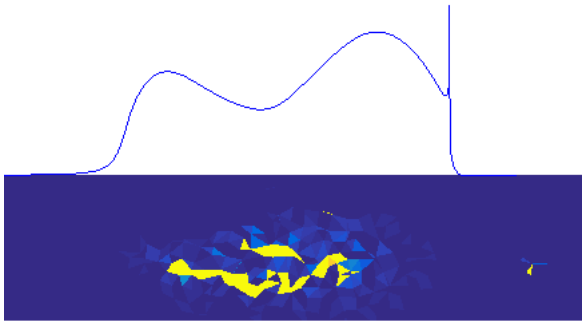

e) Load Pass 200

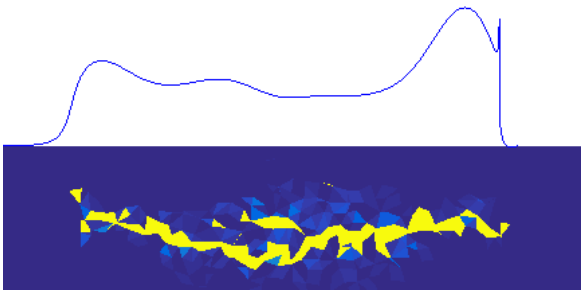

f) Load Pass 500

Figure 4: Damage and pressure profiles for the EHL pressure model showing the change in pressure with accumulated damage.

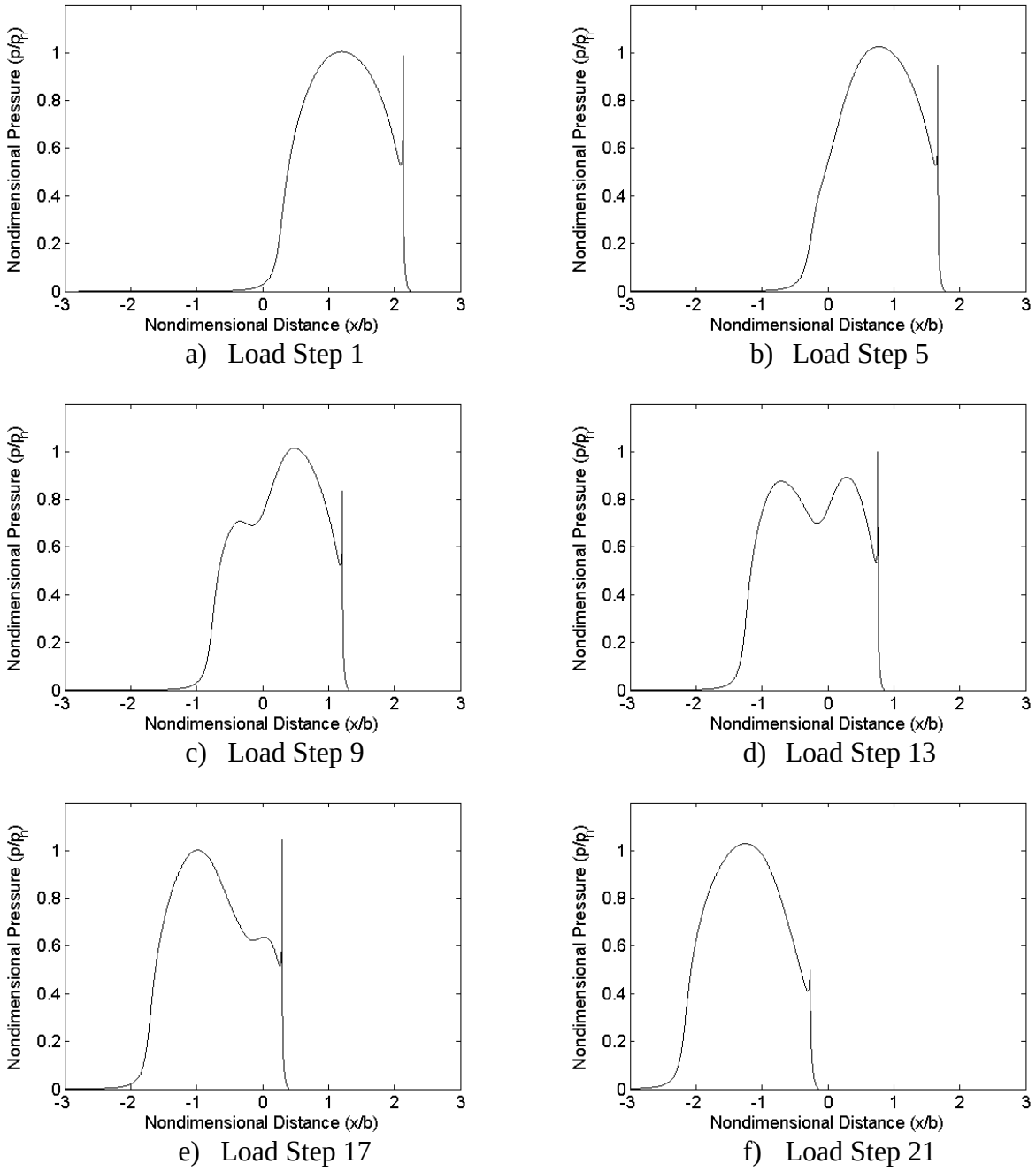

a) Load Step 1

b) Load Step 5

c) Load Step 9

d) Load Step 13

e) Load Step 17

f) Load Step 21

Figure 5: Progression of load steps in load pass 100

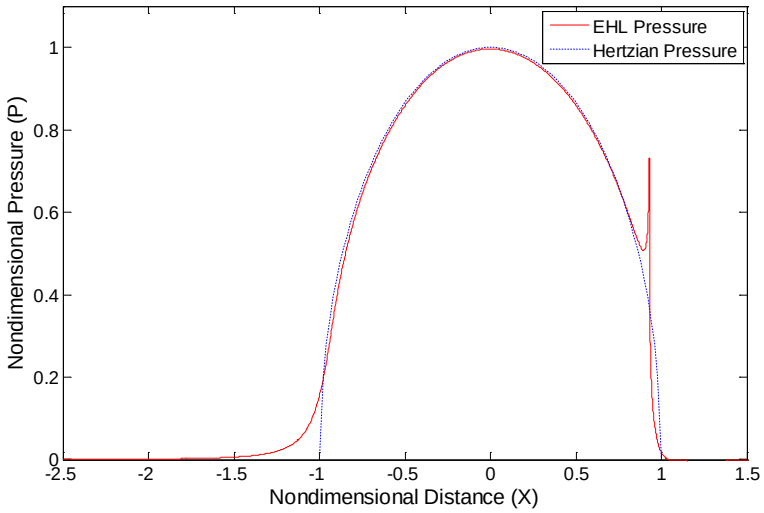

Figure 6: Comparison of Hertzian pressure to EHL pressure profiles.

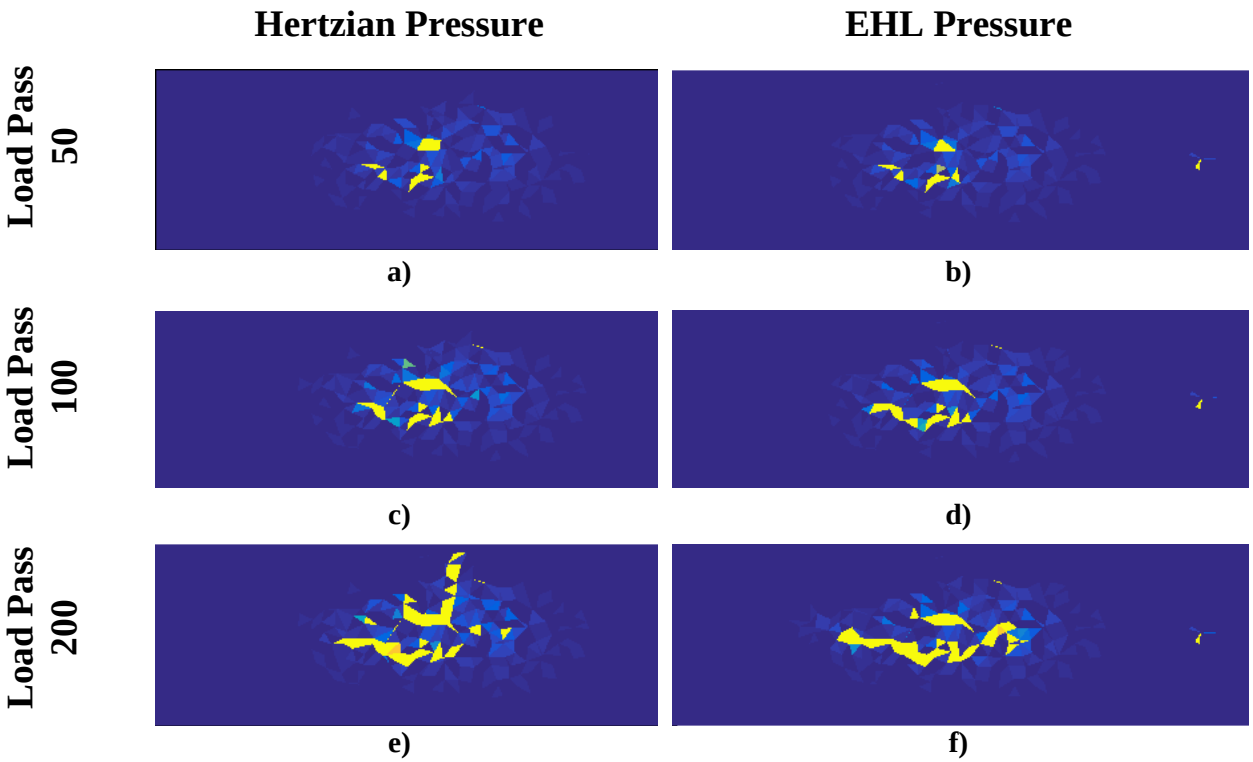

Figure 7: Comparison of Hertzian and EHL pressure profiles at different load passes.

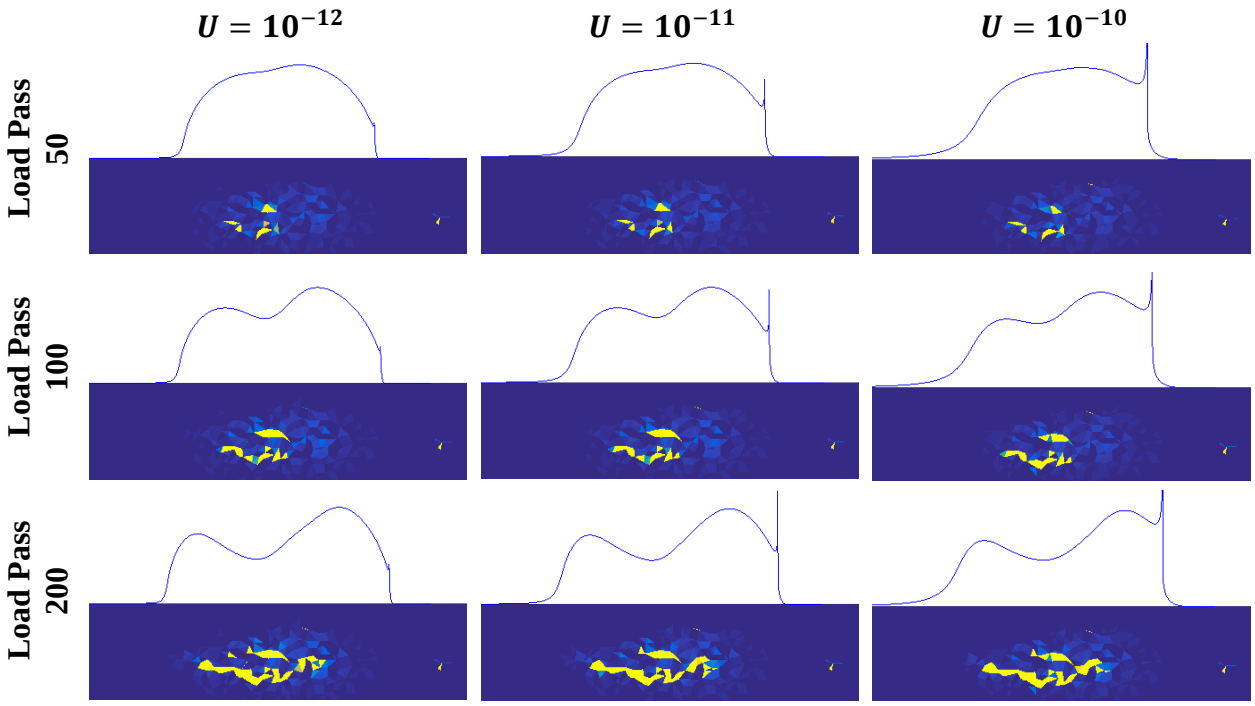

Figure 8: Effect of roller speed on the fatigue damage using the proposed EHL model

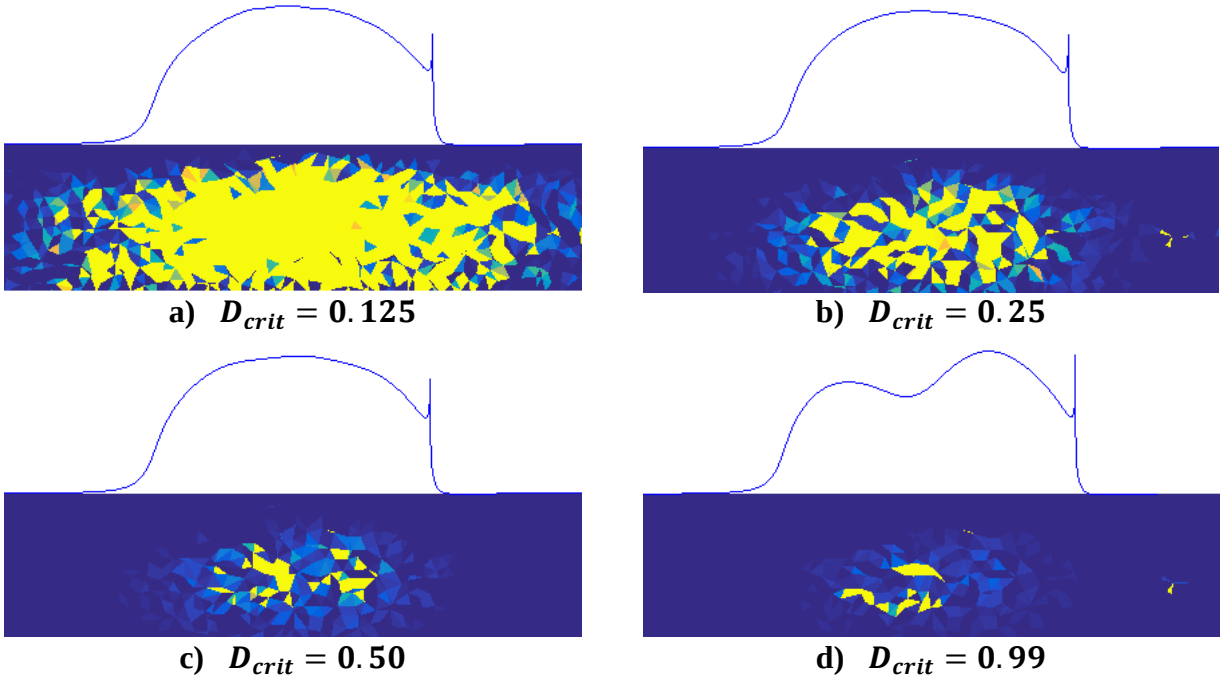

Figure 9: Critical damage value effect on damage development under rolling contact fatigue. All results shown after 100 computation load passes.